


Faraday pattern formations in temporally driven Rydberg-dressed Bose-Einstein condensatesZeyun Shi ¹, Lu Qin,² Fazal Badshah,¹ Yuan Zhou,¹ and Haibo Huang¹¹*School of Electrical and Information Engineering, Hubei University of Automotive Technology, Shiyan 442002, China*²*Department of Physics, Henan Normal University, Xinxiang, 453007, China*

(Received 3 November 2023; accepted 7 December 2023; published 27 December 2023)

We investigate both analytically and numerically the dynamics of Rydberg-dressed Bose-Einstein condensates subjected to periodic modulation of the nonlocal repulsive interactions in time through temporally modulated control laser field. We show that, by utilizing such a control laser field, the nonlocal nonlinear interactions may be tuned actively, and hence a plane-wave state of matter wave can undergo a roton instability (RI) and Faraday instability (FI) simultaneously or separately, depending on the choice of the system parameters. Specifically, based on Floquet stability analysis, we find the evolution of small perturbations of the background allows the instability growth, thereby identifying instability regions with respect to density waves. Furthermore, we find that among other modes of the system the roton mode is most effectively excited due to a significant contribution of subharmonics of the excitation frequency. From the direct numerical simulations of nonlocal Gross-Pitaevskii equation (GPE) and the Fourier analysis on profile of the density waves, we further show the frequency of temporal oscillations of density waves coincides with half of the driving frequency, which, therefore, is the evidence of the parametric resonance and is characteristic of Faraday waves. In addition, an interesting possibility would be to generate a steady stand-wave in the condensate which can persist after the creation even though canceling the modulation, and finally the two-dimensional Faraday waves are excited through manipulating local or nonlocal nonlinear coefficients in the system.

DOI: [10.1103/PhysRevA.108.063317](https://doi.org/10.1103/PhysRevA.108.063317)**I. INTRODUCTION**

Pattern formations in extended and driven systems through some dynamical instabilities are important phenomena appearing widely in nature and in literature, ranging from physics, chemistry, biology, cosmology to economics and even sociology, and so on [1,2]. Well-known examples include convection cells, fluid rolls, nematic liquid crystals, Faraday waves, snowflake pattern, Turing pattern, optical patterns, and so on [3–12]. One of the oldest and most well-known phenomena are the so-called Faraday waves [7], which refer to nonlinear standing waves appearing on liquids enclosed by a vibrating receptacle when the vibration frequency exceeds a critical value, the flat hydrostatic surface becomes unstable. Generally, in Faraday's experiment, the uniform state loses its stability against spatially or temporally modulated wave forms whose dominant length scale is determined by the intrinsic properties of the system. Advancing such research to cold atomic system is of much interest for both fundamental physics and practical applications.

In the past few decades, considerable efforts were made on the study of the above phenomena for driven pattern formation system. Bose-Einstein condensates (BECs) work as one of the ideal platform for such experimental exploration since their experimental tunability permits one to create such parametric resonance phenomena in a multiplicity of ways. One is driven by temporally modulated trap confining the system [13,14], the other is driven by modulating the scattering length by means of Feshbach resonances [15,16]. Consequently, a variety of Faraday waves are found in one or two-dimensional BECs [16–18], single or multi-component BECs [19,20], one

or two-frequency driven BECs [21,22], dipolar BECs [23,24], Fermi-Bose mixtures [25], and so on.

On the other hand, over the last two decades a large amount of research works focused on the investigation of cold Rydberg gases [26,27], where a strong long-range (nonlocal) van der Waals interaction from highly excited Rydberg atoms leads to a wide range of applications in quantum technology and science, many-body physics, synthetic quantum magnets, and quantum computation [27–30]. However, the investigation of spontaneous pattern formation induced by Faraday instabilities in the Rydberg-dressed BECs is still lacking. This motivated us to study the novel Faraday waves in Rydberg-dressed BECs with the strong long-range interaction of Rydberg atoms.

In this paper, we propose and analyze a scheme to investigate the dynamics of Rydberg-dressed BECs subject to periodic modulation of the nonlocal interactions in time through temporally modulated control laser field. The actual realization of the temporally modulated patterns arose in a somewhat different way in comparison to what described in the above studies [13–16] since the nonlocal nonlinearity is modulated. Through detailed analytical and numerical analysis, we find that by utilizing temporally modulated control laser field, the nonlocal nonlinear interactions may be tuned actively, and hence a plane-wave state of matter wave can undergo a roton instability (RI) and Faraday instability (FI) simultaneously or separately, depending on the choice of the system parameters.

Specifically, based on Floquet stability analysis, we find the evolution of small perturbations of the background allows the instability growth, thereby identifying instability regions

with respect to density waves. Meanwhile, Floquet analysis reveals that a series of resonances exist, consisting of a main resonance at half the driving frequency, and higher resonance tongues at integer multiples of half the driving frequency. Furthermore, we find that among other modes of the system the roton mode is most effectively excited due to a significant contribution of subharmonics of the excitation frequency. From the direct numerical simulations of nonlocal Gross-Pitaevskii equation (GPE), we further show the frequency of temporal oscillations of density waves coincides with half of the driving frequency, which, therefore, is the evidence of the parametric resonance and is characteristic of Faraday waves. In our numerical simulation, we can observe that the Faraday patterns emerge in a much shorter time. Interestingly, for our system, it is possible to generate a steady stand-wave in the condensate which can persist once created even after canceling the modulation. Moreover, we also realized the two-dimensional Faraday waves in our system. These investigations enriched our understanding on the driven pattern formation mechanisms of the related pattern formation in systems with repulsive long-range interactions, which has the potential applications in fundamental physics along with the practical implications.

The remainder of the article is arranged as follows. In Sec. II, we describe the physical model, drive the nonlocal GPE, and obtain the effective response function contributed from Rydberg interaction. In Sec. III, we investigate the RI of a plane-wave state and derive a Mathieu-type equation for study the FI by utilizing Floquet stability analysis. In Sec. IV, we solve numerically the GPE and find the various one- and two-dimensional Faraday density waves. The last section (Sec. V) gives a summary of our main research results.

II. PHYSICAL MODEL

We consider a system with N identical atoms, whose motion of the center of mass is quantized. The atoms have multiple internal states $|\alpha\rangle$ ($\alpha = 1, 2, 3$). As shown in Fig. 1(a), the probe laser field \mathbf{E}_p (blue, with Rabi frequency Ω_p) couples the ground state $|1\rangle$ and excited state $|2\rangle$, the control laser field \mathbf{E}_c (purple, with Rabi frequency Ω_c) couples the state $|2\rangle$ and high-excited Rydberg state $|3\rangle$. $\Delta_{2(3)}$ is the one-(two-)photon detuning, Γ_{12} and Γ_{23} are the spontaneous emission decay rates from $|2\rangle$ to $|1\rangle$ and $|3\rangle$ to $|2\rangle$, respectively. The second-quantization Hamiltonian of the system is given by

$$\begin{aligned} \hat{H} = & \int d^3r \hat{\Psi}^\dagger(\mathbf{r}) \left[-\frac{\hbar^2 \nabla^2}{2m} + V(\mathbf{r}) - \sum_{\alpha=2,3} \hbar d_\alpha |\alpha\rangle\langle\alpha| \right. \\ & \left. - \hbar \Omega_p |2\rangle\langle 1| - \hbar \Omega_c |3\rangle\langle 2| + \text{h.c.} \right] \hat{\Psi}(\mathbf{r}) + \frac{1}{2} \iint d^3r d^3r' \\ & \times \sum_{\alpha,\beta=1}^3 \hat{\psi}_\alpha^\dagger(\mathbf{r}) \hat{\psi}_\beta^\dagger(\mathbf{r}') U_{\alpha\beta}(\mathbf{r}, \mathbf{r}') \hat{\psi}_\beta(\mathbf{r}') \hat{\psi}_\alpha(\mathbf{r}), \end{aligned} \quad (1)$$

where $d^3r = dx dy dz$, ∇ is three-dimensional (3D) nabla operator on coordinate $\mathbf{r} = \{x, y, z\}$, $d_\alpha = \Delta_\alpha + i\gamma_\alpha/2$ ($\alpha = 2, 3$) with γ_α the damping, $V(\mathbf{r}) = \frac{1}{2} m \omega_\perp^2 (x^2 + y^2) + \frac{1}{2} m \omega_z^2 z^2$, with m , ω_\perp , and ω_z the center of mass of

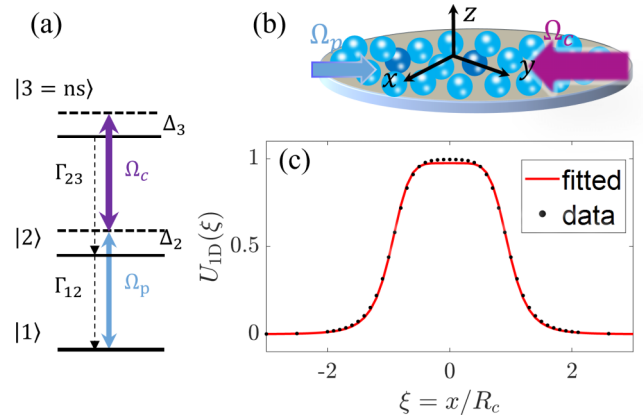


FIG. 1. Schematics of the model. (a) Ladder-type three-level atomic configuration for realizing the Rydberg-dressed BECs. The two laser fields with half Rabi frequencies Ω_p (blue) and Ω_c (purple) drive the transitions $|1\rangle \leftrightarrow |2\rangle$ and $|2\rangle \leftrightarrow |3\rangle$, respectively; $|1\rangle$, $|2\rangle$, and $|3\rangle$: ground state, excited state, and highly excited Rydberg state; $\Delta_{2(3)}$: the one-(two-) photon detuning; Γ_{12} and Γ_{23} : the spontaneous emission decay rates from $|2\rangle$ to $|1\rangle$ and $|3\rangle$ to $|2\rangle$, respectively. (b) Possible experimental geometry for disk-shaped BECs. (c) Response function $U_{ID}(\xi)$ (black spot) and its fitting result (solid red line) as a functions of the dimensionless $\xi = x/R_c$.

the atom and the trap frequencies in the xy plane and in the z axis, respectively. $U_{\alpha\beta}(\mathbf{r}, \mathbf{r}')$ is the interaction potential. The atomic annihilation operator is $\hat{\Psi}(\mathbf{r}) = \sum_\alpha \hat{\psi}_\alpha(\mathbf{r}) |\alpha\rangle$ [$\hat{\Psi}^\dagger(\mathbf{r}) = \sum_\alpha \hat{\psi}_\alpha^\dagger(\mathbf{r}) \langle\alpha|$] with $\hat{\psi}_\alpha(\mathbf{r})$ the annihilation operator of α th component. The half Rabi frequencies of the probe and control fields are, respectively, $\Omega_p = (\mathbf{e}_p \cdot \mathbf{p}_{21}) E_p / \hbar$ and $\Omega_c = (\mathbf{e}_c \cdot \mathbf{p}_{32}) E_c / \hbar$, with $\mathbf{p}_{\alpha\beta}$ the electric dipole matrix element associated with the transition between the $|\alpha\rangle$ and $|\beta\rangle$.

The Heisenberg equations of motion for $\hat{\psi}_\alpha$ ($\alpha = 1, 2, 3$) can be reduced into a Gross-Pitaevskii (quantum nonlinear Schrödinger) equation for $\hat{\psi}_1$, with a nonlocal nonlinear term representing the Rydberg-Rydberg interaction between the atoms. For details, see Appendix A. Under mean-field approximation, we have the nonlocal, c-number GPE

$$\begin{aligned} i\hbar \frac{\partial}{\partial t} \Psi(\mathbf{r}, t) = & \left[-\frac{\hbar^2 \nabla^2}{2m} + V(\mathbf{r}) + W |\Psi(\mathbf{r}, t)|^2 \right. \\ & \left. + \int U_{\text{eff}}(\mathbf{r} - \mathbf{r}') |\Psi(\mathbf{r}', t)|^2 d\mathbf{r}' \right] \Psi(\mathbf{r}, t). \end{aligned} \quad (2)$$

Here $\Psi(\mathbf{r}, t)$ is the condensate wave function, which is normalized under $N = \int |\Psi(\mathbf{r}, t)|^2 d\mathbf{r}$, and $W = 4\pi \hbar^2 a_s / m$ is the coefficient of the local interaction with a_s the s -wave scattering length. The effective long-range vdW interaction between Rydberg-dressed ground-state atoms is

$$U_{\text{eff}}(\mathbf{r} - \mathbf{r}') = \frac{\hbar \tilde{C}_6}{|\mathbf{r} - \mathbf{r}'|^6 + R_c^6}, \quad (3)$$

where the effective dispersion parameter and blockade radius are $\tilde{C}_6 = |\Omega_c|^4 |\Omega_p|^4 C_6 / |D|^4$ and $R_c = (NC_6 d_2 |\Omega_c|^2 |\Omega_p|^2 / |D|^2 D)^{1/6}$, respectively. The detailed derivation is given in Appendix A. Equation (2) can be cast

into the dimensionless form

$$\begin{aligned}
 & i \frac{\partial}{\partial \tau} \psi_{3D}(\boldsymbol{\rho}, \tau) \\
 &= \left[-\frac{1}{2} \tilde{\nabla}^2 + V(\boldsymbol{\rho}) \right] \psi_{3D}(\boldsymbol{\rho}, \tau) + w_1 |\psi_{3D}|^2 \psi_{3D} \\
 &+ w_2 \int U_{3D}(\boldsymbol{\rho} - \boldsymbol{\rho}') |\psi_{3D}(\boldsymbol{\rho}', \tau)|^2 d^3 \rho' \psi_{3D}(\boldsymbol{\rho}, \tau), \quad (4)
 \end{aligned}$$

where $\Psi(\mathbf{r}, t) = \psi_{3D}(\boldsymbol{\rho}, \tau) \sqrt{N/R_c^3}$, $\tau = t/\tau_0$ ($\tau_0 = mR_c^2/\hbar$), $\boldsymbol{\rho} = (\xi, \eta, s) = (x, y, z)/R_c$, $\tilde{\nabla}^2 = \partial^2/\partial \xi^2 + \partial^2/\partial \eta^2 + \partial^2/\partial s^2$, $V(\boldsymbol{\rho}) = \frac{1}{2} \tau_0^2 [\omega_x^2 \xi^2 + \omega_y^2 \eta^2 + \omega_z^2 s^2]$, $w = 4\pi a_s N/R_c$, $w_2 = Nm\tilde{C}_6/(\hbar R_c^4)$, and $U_{3D}(\boldsymbol{\rho}) = 1/(1 + |\boldsymbol{\rho}|^6)$.

To further simplify the analysis, we consider a one-dimensional (1D) geometry which assumes a strong confinement in the radial (yz) plane, i.e., $\omega_{y,z} \gg \omega_x$. In this case, the dynamics of the BEC in the radial plane is confined in the ground state, $\phi(\eta, s) = \frac{1}{\sigma_z \sqrt{\pi}} \exp[-(\eta^2 + s^2)/(2\sigma_z^2)]$. Now, we have the wave function $\psi_{3D}(\boldsymbol{\rho}, \tau) = \phi(\eta, s) \psi(\xi, \tau)$, where $\psi(\xi, \tau)$ is the effective 1D wave function for the radial dynamics. To derive the effective 1D equation for the Rydberg dressed BEC, we insert ansatz into Eq. (4), multiply by the ground-state wave function $\phi(\eta, s)$ and integrate over η and s to get the 1D equation

$$\begin{aligned}
 & i \frac{\partial}{\partial \tau} \psi(\xi, \tau) = \left[-\frac{1}{2} \frac{\partial^2}{\partial \xi^2} + V(\xi) + w_1 |\psi|^2 \right] \psi(\xi, \tau) \\
 &+ w_2 \int U_{1D}(\xi - \xi') |\psi(\xi', \tau)|^2 d\xi' \psi(\xi, \tau), \quad (5)
 \end{aligned}$$

where $V = \frac{1}{2} \tau_0^2 \omega_x^2 \xi^2$, $w_1 = 2a_s N/(R_c \sigma_z^2)$ could be positive or negative, depending on the choice of s -wave scattering length a_s , which can be adjusted actively by optically [31] or magnetically [32,33] induced Feshbach resonance. $U_{1D}(\xi) = \int U_{3D}(\boldsymbol{\rho}) |\phi(\eta, s)|^2 d\eta ds$ is the one-dimensional effective response function, and the linear term $b\psi$ with $b = \frac{1}{4} [\frac{2}{\sigma_z^2} + \tau_0^2 (\omega_y^2 + \omega_z^2) \sigma_z^2]$ is eliminated by using a phase transformation $\psi \rightarrow \psi e^{-ibr}$. Here we choose $a_s < 0$ for attractive contact interaction to guarantee the roton instability to happen easily (which will be discussed in the following) and w_2 depends on the Rydberg state.

To realize the model, one may choose a cold ^{87}Rb atom as a realistic example. The assigned atomic levels are [34] $|1\rangle = |5S_{1/2}, F=1, m_F=0\rangle$, $|2\rangle = |5P_{3/2}, F=1, m_F=0\rangle$, and $|3\rangle = |nS_{1/2}\rangle$. The system parameters are $\Gamma_{23} = 2\pi \times 3.1$ MHz, $\Gamma_{12} = 2\pi \times 1.0$ kHz, $\Delta_2 = 2\pi \times 100$ MHz, $\Delta_3 = 2\pi \times 30$ MHz, $\Omega_c = 2\pi \times 14$ MHz, and $\Omega_p = 2\pi \times 5$ MHz, respectively. For principle quantum number $n = 60$, $C_6 = -2\pi \times 140$ GHz μm^6 (the Rydberg-Rydberg interaction is repulsive) [35].

For the sake of convenience and clarity in discussion, the effective 1D response function $U_{1D}(\xi)$ is fitted by $U_{1D}(\xi) \approx 0.78/(0.80 + |\xi|^6)$. Figure 1(c) shows the effective one-dimensional response function with the variation of ξ . Here the black dotted line is for the analytic result, which is fitted approximately as shown in red solid line.

III. ROTON INSTABILITY AND FARADAY INSTABILITY

The density waves in Rydberg dressed BECs can be induced by periodic modulation of the parameter w_1 or w_2 in Eq. (5), through a_s (via Feshbach resonance of magnetic field) and control field Ω_c (called an optical Feshbach resonance), respectively, which is well known in fluid, i.e., Faraday waves [7]. The methods are independently tunable, next we assume that the nonlocal interactions w_2 is modulated periodically, which takes the form

$$w_2 = w_{20}[1 + 2\alpha \cos(2\omega\tau)]. \quad (6)$$

Here α characterizes modulated amplitude and 2ω represents the modulated frequency. In the absence of modulation ($\alpha = 0$), the system returns to plane-wave state due to the repulsive interaction.

Meanwhile, we note that there are two types of instability that may occur in the system. One is roton instability, which occurs when system parameters satisfies some conditions due to the long-range, repulsive Rydberg-Rydberg interaction between atoms, already considered in Refs. [36–40]; the other one is Faraday instability, which occurs when periodic modulation of the parameter is applied even when the atom-atom interaction is not long-ranged (but repulsive) one, already considered before for conventional BECs in Ref. [15]. Here we are interested in both the RI and FI in Rydberg-dressed BECs.

A. Roton instability

We first assume $V(\xi) = 0$ in GPE (5) to explore the RI. In this case the GPE has the homogenous plane wave solution: $\psi_{pw}(\xi, \tau) = A_0 \exp(i\tau\alpha)$, where $A_0^2 = 1/\int d\xi$ and $\alpha = -A_0^2[w_1 + w_2 \int U_{1D}(\xi) d\xi]$. Since any perturbation can be expanded as a superposition of many Fourier modes, we make the RI analysis of the plane wave by taking only a periodic mode as the perturbation. Therefore, the perturbation solution can be expressed as $\tilde{\psi}(\xi, \tau) = [A_0 + a_1 e^{i\beta\xi - i\lambda\tau} + a_2^* e^{-i\beta\xi + i\lambda^*\tau}] e^{i\alpha\tau}$, where a_1 and a_2 are small complex amplitudes of the perturbation, $\beta \equiv R_c k_x$ is the non-dimensional wave vector (k_x is wave number in the x direction), and λ is the growth rate of the perturbation, to be determined yet.

Substituting the perturbation solution into Eq. (5) and keeping only linear terms of a_1 and a_2 , we obtain

$$\lambda^2 = \beta^2 \left\{ \frac{1}{4} \beta^2 + A_0^2 [w_1 + w_{20} \mathcal{U}_{1D}(\beta)] \right\}, \quad (7)$$

where $\mathcal{U}_{1D}(\beta)$ is the response function of U_{1D} in momentum space. We see from the above expression that the property of the growth rate λ depends on the plane-wave amplitude A_0 , the local and nonlocal nonlinear coefficients w_1 and w_{20} . To illustrate them, Fig. 2 has shown the growth rate $-\lambda^2$ for different sets of parameters β , A_0 , w_1 , and w_{20} . First, when $A_0 = 1.5$, $w_{20} = 1$, and choosing different $w_1 = -0.6, -0.9, -1.03, -1.1$, λ^2 is dramatically changed with w_1 as shown in Fig. 2(a). When $|w_1|$ is small, the curve is monotonic, however, it describe a nonmonotonic behavior as $|w_1|$ increases. Specifically, it has a connect point with x axis at $\beta_{\text{rot}} \approx 2.73$ and $\lambda = 0$ when $w_1 = -1.03$. With the further increase in $|w_1|$, the growth rate becomes pure imaginary ($\lambda^2 < 0$) and RI appears, which is the main reason for the

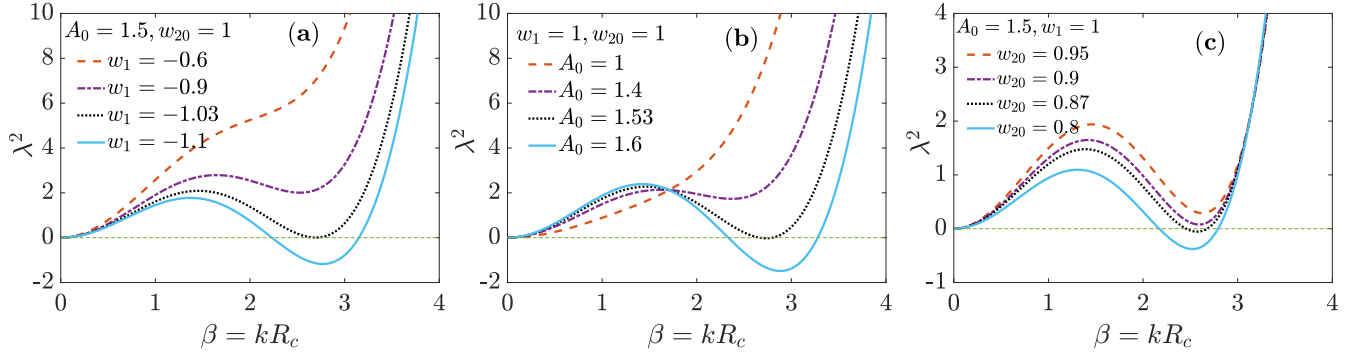


FIG. 2. λ^2 of a Rydberg-dressed BECs as a function of the dimensionless wave number $\beta = kR_c$ for different sets of parameters A_0 , w_1 , and w_{20} . (a) $A_0 = 1.5$, $w_{20} = 1$, and $w_1 = -0.6, -0.9, -1.03, -1.1$; (b) $w_1 = -1$, $w_{20} = 1$, and $A_0 = 1, 1.4, 1.53, 1.61$; and (c) $A_0 = 1.5$, $w_1 = -1$, and $w_{20} = 0.95, 0.9, 0.87, 0.8$. They are represented, respectively, by dashed red, dashed-dotted purple, dotted black, and solid blue lines.

formation of patterns in long-range repulsive nonlinear interaction systems [41–44]. Furthermore, we also see that it is a short-wave instability.

To obtain further insight of the RI, we adjust the parameters A_0 and w_{20} and fix other parameters to obtain the growth rate λ , which are shown in Fig. 2(b) with $w_1 = -1$, $w_{20} = 1$, $A_0 = 1, 1.4, 1.53, 1.61$ and Fig. 2(c) with $A_0 = 1.5$, $w_1 = -1$, $w_{20} = 0.95, 0.9, 0.87, 0.8$, respectively. They are represented by dashed red, dashed-dotted purple, dotted black, and solid blue lines. According to RI analysis, we know the state of matter wave depends on the choice of parameters, which will be discussed in the following sections.

B. Faraday instability

We now study the FI. To study the emergence and dynamics of density waves, we introduce weak perturbation of the uniform state [by setting $V(\xi) = 0$] given by Eq. (5) and look for a solution in the form

$$\psi = [A_0 + \epsilon A_1(\xi, \tau)] \exp(i\alpha\tau), \quad A_1 \ll A_0, \quad (8)$$

where A_1 is a complex function of ξ and τ . The equation for the perturbation is obtained by substituting Eq. (8) into Eq. (5) and keeping only the linear terms on A_1 , which satisfies

$$i \frac{\partial A_1}{\partial \tau} = -\frac{1}{2} \frac{\partial^2 A_1}{\partial \xi^2} + A_0^2 w_1 (A_1 + A_1^*) + A_0^2 w_2 \int U_{1D}(\xi - \xi') [A_1(\xi') + A_1^*(\xi')] d\xi'. \quad (9)$$

By representing $A_1 = B_1 + iB_2$ and separating the real and imaginary parts, we can cancel the component B_2 and get the Mathieu-type equation for B_1 in momentum space, i.e.,

$$\frac{d^2 \tilde{B}_1}{d\tau^2} + [\lambda^2 + 2\alpha A_0^2 w_{20} \beta^2 \mathcal{U}_{1D}(\beta) \cos(2\omega\tau)] \tilde{B}_1 = 0, \quad (10)$$

where \tilde{B}_1 and \mathcal{U}_{1D} are the Fourier transform of B_1 and U_{1D} . Remarkably, when $\alpha \neq 0$, the system is driven by a periodic force with frequency 2ω and amplitude $A_0^2 w_{20} \alpha \beta^2 \mathcal{U}_{1D}$. A similar equation in the context of Faraday waves in general BECs was derived in Ref. [15], but here we extended the result of that work by taking into consideration the long-ranged Rydberg-dressed atom-atom interactions.

Since the coefficient of the differential equation is a periodic function with a minimal period $T = \pi/\omega$, one can use the Floquet theory to analyze the stability properties of this system (10) (the detailed method is given in Appendix B). Furthermore, we know from Eq. (10) that the FI depends on the parameters A_0 , w_1 , α , and β . For different values of these parameters, we can find the domains of instability in the parameter space against the generation of patterns in Rydberg BECs.

Figure 3 shows the phase diagram of the domains of Faraday instability in the space of two typical parameters α and ω by varying A_0 . Figure 3(a1) is the unstable regions (red regions) as a function of α and ω for $A_0 = 1.4$, $w_1 = -1$, $w_{20} = 1$, and $\beta = 2.73$. One can see that there are different FI regions around $\omega \approx 0.748$, $\omega \approx 0.497$, and $\omega \approx 0.37$. For the appearance of FI, a larger driven amplitude α is needed

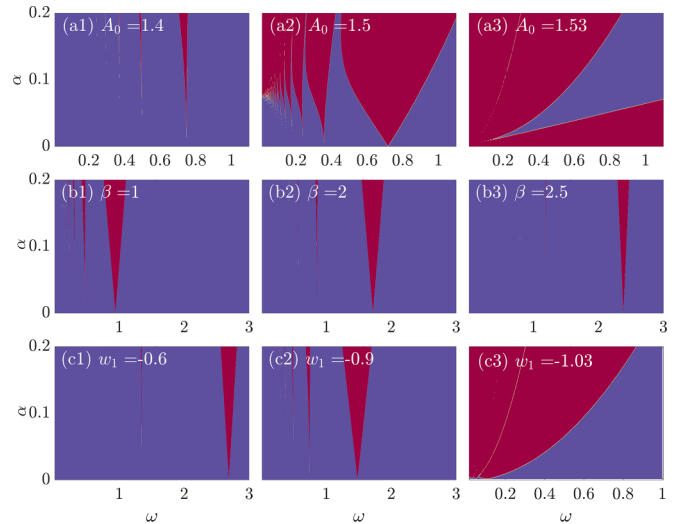


FIG. 3. Phase diagram of the domains of the Faraday instability (red regions) in the parameter space of the amplitude α and the dimensionless frequency ω of the periodic drive. (a1)–(a3): $w_{20} = 1$, $w_1 = -1$, $\beta = 2.73$, and varying $A_0 = 1.4, A_0 = 1.5$, and $A_0 = 1.53$. (b1)–(b3): $w_{20} = 1$, $w_1 = -1$, $A_0 = 1$, and varying $\beta = 1, \beta = 2$, and $\beta = 2.5$. (c1)–(c3): $w_{20} = 1$, $\beta = 2.73$, $A_0 = 1$, and varying $w_1 = -0.6, w_1 = -0.9$, and $w_1 = -1.03$.

in case of the smaller driven frequency ω . Here the colorful region is the one that FI appears. We furthermore increase A_0 to 1.5 and 1.53, many new FI regions appear, as shown in Figs. 3(a2) and 3(a3). A comparison of these figures indicates that FI occurs easily in low (high)-frequency region when A_0 is large (small). In addition, the whole parameter space becomes FI when $A_0 = 1.53$ [Fig. 3(a3)]. This is because under these circumstances, the RI also happens, which can be seen from Fig. 2(b). Therefore, under the circumstances, the system allows RI and FI, which can take action in the system jointly and simultaneously.

The FI is also affected by other system parameters. Next, we plot the FI regions as functions of α and ω for different $\beta = 1, 2$, and 2.5, respectively, when $A_0 = 1$, $w_{20} = 1$, and $w_1 = -1$ in Figs. 3(b1) to 3(b3). It represents that FI happens in low (high)-frequency region when β is small (large). In addition, we can control Faraday instability by changing w_1 , which are drawn as functions of α and ω for different $w_1 = -0.6, -0.9$, and -1.03 , respectively, when $A_0 = 1$, $w_{20} = 1$, and $\beta = 2.73$ in Figs. 3(c1) to 3(c3).

Therefore, due to the long-ranged Rydberg-Rydberg interactions and the Faraday driving, the system allows both RI and FI, which can take action in the system jointly and simultaneously. The cooperation and competition between the RI and FI may display very rich and interesting phases. Further comparing Figs. 2 and 3, we find that in the limiting case of very small α , the system displays only RI; on the contrary, in the limiting case of not large A_0 , the system displays only FI. Further, for the intermediate case, the system displays a new kind of instability (joint RI-FI) that different from both the RI and FI. In the following, we will explore the output of RI and FI, respectively.

IV. FARADAY PATTERN FORMATION

A. 1D Faraday pattern formation through manipulating w_2

Based on Faraday instability analysis, we solved Eq. (5) numerically. The starting point is the perturbed ground state of Eq. (8), which is numerically obtained by the split Fourier method under the periodic boundary conditions. The number of Fourier modes and time step are $N_F = 2^{12}$ and $\Delta\tau = 0.0001$, respectively. The integration domain is selected to be sufficiently large $\xi \in [-75\pi, 75\pi]$ to accommodate many periods of emerging waves on average. When the amplitude of a density wave starts to increase rapidly due to a parametric resonance, typically exceeding 20% of the background amplitude, we interrupt the numerical simulation and analyze the resulting spatial pattern. As a rule, the spatial pattern represents a superposition of waves with different spatial periods and displays as a high-frequency component modulated by a low-frequency envelope. Modulation of the amplitude originates from constructive and destructive interference of emerging density waves with different periods.

As an example, we first solve the Eq. (5) with parameters $A_0 = 1.4$, $w_{20} = 1$, $w_1 = -1$, $\omega = 0.748$ [which is obtained from Fig. 3(a), the most unstable frequency component], and $\alpha = 0.05$. The corresponding density waves are illustrated in Fig. 4(a). Here for obtaining the result, we plot the difference $|\psi(\xi, \tau)| - A_0$ as a function of ξ and τ , where the red (blue)

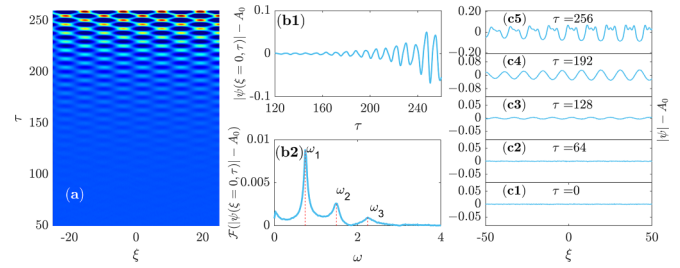


FIG. 4. Creation of density waves by time modulated periodically nonlocal interaction with parameters $A_0 = 1.4$, $w_{20} = 1$, $w_1 = -1$, $\omega = 0.748$, and $\alpha = 0.05$. (a) $|\psi(\xi, \tau)| - A_0$ as functions of $\xi = x/R_c$ and $\tau = t/\tau_0$, where the red (blue) region represents the large (small) value. (b1) Density wave $|\psi(\xi = 0, \tau)| - A_0$ at central position $\xi = 0$ as a function of time τ , and (b2) its power spectrum $\mathcal{F}(|\psi(\xi = 0, \tau)| - A_0)$ as a function of frequency ω , which consists mainly of three frequencies, i.e., $\omega_1 = 0.748$ (half of driven frequency), $\omega_2 = 1.496 \approx 2\omega_1$, and $\omega_3 = 2.24 \approx 3\omega_1$. (c1)–(c5) Density wave at some particular time instances, i.e., $\tau = 0, 64, 128, 192$, and 256.

region represents the large (small) value. It suggests that the GPE (5) may have a superposition of the different periodic solutions. To verify this conjecture, we pick a density wave at some particular space, namely, at $\xi = 0$ [shown in Fig. 4(b1)], and at some particular time instances, i.e., $\tau = 0, 64, 128, 192$, and 256 [shown in Figs. 4(c1)–4(c5)]. We can see that the density wave is periodic both in time and space, and it consists of multiple harmonics. Furthermore, the amplitude of the waves increases with the duration of the driving. Specifically, we plot the power spectrum of Fig. 4(b1) for density wave at $\xi = 0$ in Fig. 4(b2), which mainly includes three frequencies, i.e., $\omega_1 = 0.748$ (the half of driven frequency), $\omega_2 \approx 2\omega_1$, and $\omega_3 \approx 3\omega_1$. It illustrates that the wave consists of three harmonics in time, and is evidence of the parametric resonance phenomenon [45].

Next, the driven frequency is adjusted to $\omega = 0.497$ [corresponding to the second Faraday unstable band in Fig. 3(a)] while other parameters remain unchanged, and we solved Eq. (5) again. Here we also plot the difference $|\psi(\xi, \tau)| - A_0$ as a function of ξ and τ , where the red (blue) region represents the large (small) value in Fig. 5(a). We choose a density wave at some particular space, namely, at $\xi = 0$ [shown in Fig. 5(b1)], and at some particular time instances, i.e., $\tau = 0, 200, 300, 350$, and 424.5 [shown in Figs. 5(c1) to 5(c5)]. The density wave is also periodic both in time and space, and it consists of multiple harmonics. Specifically, we plot the power spectrum of Fig. 5(b1) for density wave at $\xi = 0$ in Fig. 5(b2), which mainly includes two frequencies, i.e., $\omega_1 = 0.497$ (the half of driven frequency) and $\omega_2 \approx 2\omega_1$. It illustrates that the wave consists of two harmonics with approximately same amplitudes in time.

Comparing the simulation results illustrated in Figs. 4 and 5, we identified distinct features of the density waves. For instance, the later effective excitation needs a much longer time. While the amplitudes of two excitation frequencies are basically equal to each other for later case but different for the previous. In addition, the distribution of wave patterns is also different with each other.

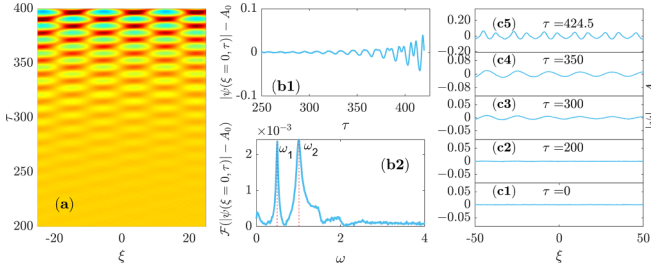


FIG. 5. Creation of density waves by time modulated periodically nonlocal interaction with dimensionless parameters $A_0 = 1.4$, $w_{20} = 1$, $w_1 = -1$, $\omega = 0.497$, and $\alpha = 0.05$. (a) Density difference $|\psi(\xi, \tau)| - A_0$ as functions of $\xi = x/R_c$ and $\tau = t/\tau_0$, where the red (blue) region represents the large (small) value. (b1) Density wave $|\psi(\xi = 0, \tau)| - A_0$ at central position $\xi = 0$ as a function of time τ , and (b2) the corresponding power spectrum $\mathcal{F}(|\psi(\xi = 0, \tau)| - A_0)$ as function of frequency ω , which consists mainly of two frequencies, i.e., $\omega_1 = 0.497$ (half of driven frequency), and $\omega_2 = 1.496 \approx 2\omega_1$. (c1)–(c5) Density wave at some particular time instances, i.e., $\tau = 0, 200, 300, 350$, and 424.5 .

We further carry out the simulation with a much lower driven frequency $\omega = 0.372$ [corresponding to the third Faraday unstable band in Fig. 3(a)] and other parameters remains unchanged, which are shown in Fig. 6. A new kind of density wave pattern appears here, which shapes the prismatic structures. Here $|\psi(\xi, \tau)| - A_0$ as functions of ξ and τ are shown in Fig. 6(a) with the red (blue) region representing the large (small) value. Meanwhile, we plot $|\psi(\xi = 0, \tau)| - A_0$ in Fig. 6(b1) and its power spectrum in Fig. 6(b2) for the density wave. This pattern consists principally of one frequency $\omega_1 = \omega = 0.372$. By choosing a density wave at some particular time instances, i.e., $\tau = 0, 200, 300, 350$, and 424.5 , we obtain some profiles shown in Figs. 6(c1) to 5(c5).

The patterns can be controlled not only by the driven frequency, but also the parameters of the system, e.g., A_0 . We now simulate numerically GPE (5) by increasing A_0 to 1.5 and changing the driven frequency $\omega = 0.72$ [corresponding to Fig. 3(b)]. Figure 7 displays the density wave and some

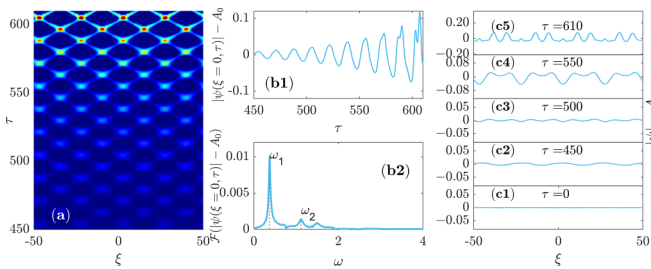


FIG. 6. Creation of density waves by time modulated periodically nonlocal interaction with $A_0 = 1.4$; $w_{20} = 1$, $w_1 = -1$, $\omega = 0.372$, and $\alpha = 0.05$. (a) Density difference $|\psi(\xi, \tau)| - A_0$ as functions of $\xi = x/R_c$ and $\tau = t/\tau_0$, where the red (blue) region represents the large (small) value. (b1) $|\psi(\xi = 0, \tau)| - A_0$ at central position $\xi = 0$ as a function of time τ , and (b2) its power spectrum $\mathcal{F}(|\psi(\xi = 0, \tau)| - A_0)$ as a function of frequency ω , which consists principally of one frequency, i.e., $\omega_1 = 0.372$ (half of driven frequency). (c1)–(c5) Density wave at some particular time instances, i.e., $\tau = 0, 450, 500, 550$, and 610 .

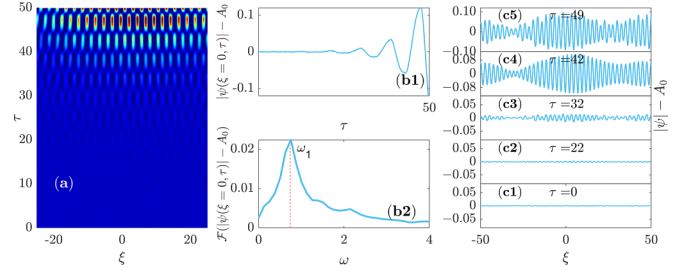


FIG. 7. Creation of density waves by time modulated periodically nonlocal interaction with $A_0 = 1.5$; $w_{20} = 1$, $w_1 = -1$, $\omega = 0.72$, and $\alpha = 0.01$. (a) Density difference $|\psi(\xi, \tau)| - A_0$ as functions of $\xi = x/R_c$ and $\tau = t/\tau_0$, where the red (blue) region represents the large (small) value. (b1) Density wave $|\psi(\xi = 0, \tau)| - A_0$ at central position $\xi = 0$ as a function of time τ , and (b2) the corresponding power spectrum $\mathcal{F}(|\psi(\xi = 0, \tau)| - A_0)$ as function of frequency ω , which consists principally of one frequency, i.e., $\omega_1 = 0.72$ (half of driven frequency). (c1)–(c5) Density wave at some particular time instances, i.e., $\tau = 0, 22, 32, 42$, and 49 .

particular profile in space and time. Here $|\psi(\xi, \tau)| - A_0$ as a function of ξ and τ is shown in Fig. 7(a), which is very different from Figs. 4–6. We find that it just needs a driving with very short duration. Meanwhile, it suggests that the GPE (5) may have a standing-wave-type spatially periodic solution under these conditions. Furthermore, it creates an effective driving with oscillating frequency $\omega_1 = \omega = 0.72$, which are shown in Figs. 7(b1) and 7(b2). For clarity, we also plot the specific wave profile at different time $\tau = 0, 140, 190, 240$, and 290 in Figs. 7(c1) to 7(c5). We see clearly that the emerging density wave represents a superposition of many wave components. Constructive and destructive interference of these components produce a picture where a high-frequency wave appears to be modulated by a low-frequency envelope. From the FI analysis in Fig. 3, one can also generate some other novel density wave patterns by varying the amplitude A_0 , nonlinear coefficient w_1 and w_2 , modulated wave number β , and so on. For saving space, we do not display them here.

An interesting possibility would be to generate a steady wave in the condensate, which can persist once created even after canceling the modulation. To serve the purpose, we performed numerical experiments in which the periodic modulation in GPE (5) was kept until some time instance τ_0 and after that was set to zero, i.e., $\alpha = 0$ when $\tau > \tau_0$. For example, we set $\tau_0 = 30$, and other parameters are the same as that in Fig. 7, which is illustrated in Fig. 8(a). The result for the density wave is shown in Fig. 8(b). As can be seen, the density waves are preserved after creation, provided that the modulation of the coefficient of α ceases at some point in time $\tau = 30$. It is the expected outcome since the original model GPE (5) is conservative. However, we should stress that in real experimental settings some dissipation effects may be present, leading to a damping of density waves, but these issues are beyond of the scope of present work.

B. 2D Faraday pattern formation through manipulating w_2

When we relax the confinement in y direction, Eq. (5) becomes a $(2 + 1)$ D GPE with the nonlocal nonlinear

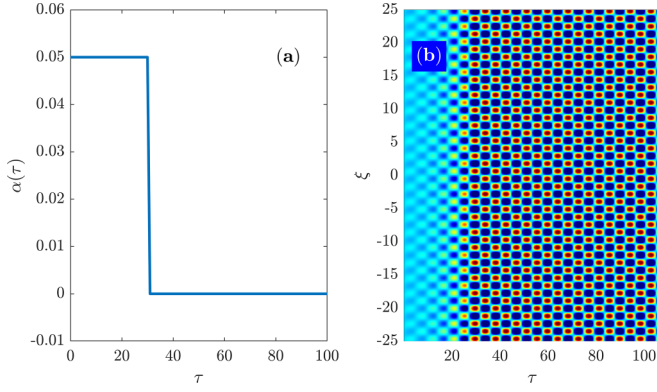


FIG. 8. (a) Profile of the modulated parameter α . (b) Creation of density wave $|\psi(\xi, \tau)| - A_0$ by time modulated periodically nonlocal interaction with $A_0 = 1.5$; $w_{20} = 1$, $w_1 = -1$, $\omega = 0.72$, and $\alpha = 0.05$ when $\tau < 30$, which as functions of $\xi = x/R_c$ and $\tau = t/\tau_0$, where the red (blue) region represents the large (small) value.

modulation in temporal [replace $\partial^2/\partial\xi^2$ by $\partial^2/\partial\xi^2 + \partial^2/\partial\eta^2$]. We now investigate the dynamics of the system by solving the (2 + 1)D GP equation numerically through the pseudo-spectral method and random initial conditions. In the simulation, the corresponding parameters are chosen as $A_0 = 1.5$; $w_{20} = 1$, $w_1 = -1$, $\omega = 0.72$, and $\alpha = 0.05$. Figure 9 displays the results of two-dimensional density waves $|\psi(\vec{\zeta}, \tau)|^2$ as a function of ξ and η for different times $\tau = 50, 196, 332$, and 375 in the top row [Figs. 9(a1) to 9(a4)] and their Fourier transform in the momentum space $|\hat{\psi}(\vec{\beta}, \tau)|^2$ in the bottom row [Figs. 9(b1) to 9(b4)]. Here the red (blue) region represents the large (small) value. It can be seen that the homogenous density wave is modulated first in the η direction to form the stripe structure [Fig. 9(a2)] and then modulated in the ξ direction to form the square structure [Fig. 9(a4)].

Furthermore, we simulate the (2 + 1)D GP equation numerically through choosing the parameters $A_0 = 1.0$; $w_{20} = 1$, $w_1 = -0.6$, $\omega = 2.73$, and $\alpha = 0.05$, some novel Faraday waves are found, which are illustrated in Fig. 10. Specifically,

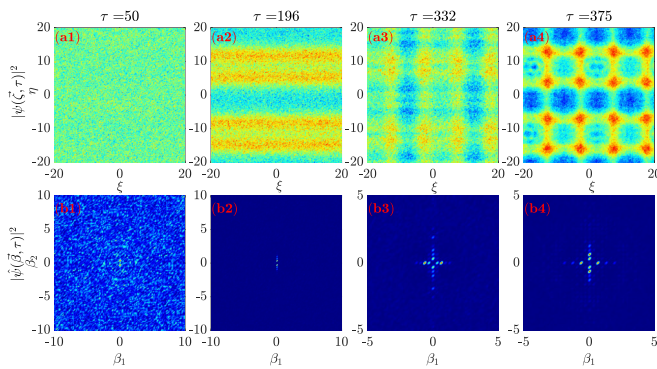


FIG. 9. Creation of two-dimensional density wave $|\psi(\vec{\zeta}, \tau)|^2$ by time modulated periodically nonlocal interaction with $A_0 = 1.5$; $w_{20} = 1$, $w_1 = -1$, $\omega = 0.72$, and $\alpha = 0.05$ for different time $\tau = 50, 196, 332$, and 375 in (a1)–(a4), and that in the momentum space $|\hat{\psi}(\vec{\beta}, \tau)|^2$ with $\vec{\beta} \equiv (\beta_1, \beta_2) = R_c(k_1, k_2)$ in (b1)–(b4), where the red (blue) region represents the large (small) value.

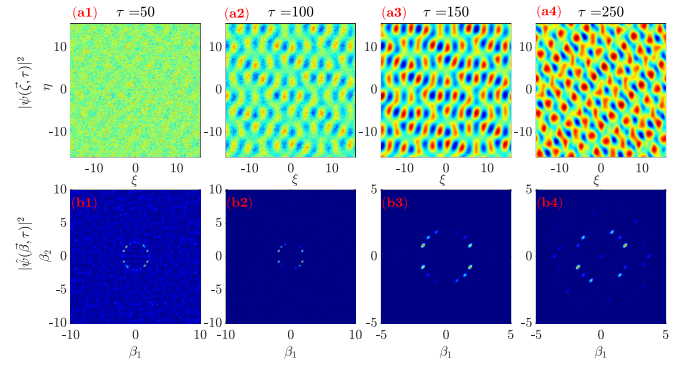


FIG. 10. Creation of two-dimensional density wave $|\psi(\vec{\zeta}, \tau)|^2$ by time-modulated periodically nonlocal interaction with $A_0 = 1.5$; $w_{20} = 1$, $w_1 = -0.6$, $\omega = 2.73$, and $\alpha = 0.05$ for different time $\tau = 50, 100, 150$, and 250 in (a1)–(a4), and that in the momentum space $|\hat{\psi}(\vec{\beta}, \tau)|^2$ with $\vec{\beta} \equiv (\beta_1, \beta_2)$ in (b1)–(b4), where the red (blue) region represents the large (small) value.

the results of two-dimensional density waves $|\psi(\vec{\zeta}, \tau)|^2$ as functions of ξ and η with varying time $\tau = 50, 196, 332$, and 375 in the top row [Figs. 10(a1) to 10(a4)] and their Fourier transform in the momentum space $|\hat{\psi}(\vec{\beta}, \tau)|^2$ in the bottom row [Figs. 10(b1) to 10(b4)]. Here the red (blue) region represents the large (small) value. For other parameters, some new pattern can also appear, which are not shown here for space.

C. 2D Faraday pattern formation through manipulating w_1

In the previous section, we assumed that the nonlocal nonlinearity is modulated periodically in time and keeping the scattering lengths (i.e., local nonlinearity) fixed. Here, we study the Faraday wave through manipulating the local nonlinearity, i.e., assuming $w_1 = w_{10}[1 + 2\alpha \cos(2\omega\tau)]$. Performing the analysis similar to the previous section, we obtain the Mathieu-type equation for B_1 in momentum space, which is of the form

$$\frac{d^2 \tilde{B}_1}{d\tau^2} + [\lambda^2 + 2\alpha A_0^2 w_{10} \beta^2 \cos(2\omega\tau)] \tilde{B}_1 = 0, \quad (11)$$

where \tilde{B}_1 is modulated periodically with modulation amplitude $2\alpha A_0^2 w_{10} \beta^2$ and period 2ω . Figure 11 shows the phase diagram of the domains of Faraday instability in the space of two typical parameters α and ω with other parameters $A_0 = 1.4$, $w_1 = -1$, $w_{20} = 1$, and $\beta = 2.73$, where the red regions present the unstable regions. One can see that there are different FI regions around $\omega \approx 0.71$, $\omega \approx 0.35$, $\omega \approx 0.24$, $\omega \approx 0.18$, and so on. For the appearance of FI, a larger driven amplitude α is needed in case of the smaller driven frequency ω .

Based on the FI analysis, we carry out the simulation directly on the (2 + 1)D GPE with the local nonlinear modulation in temporal by $w_1 = w_{10}[1 + 2\alpha \cos(2\omega\tau)]$. Figures 12–14 display the results of two-dimensional density waves $|\psi(\vec{\zeta}, \tau)|^2$ as a function of ξ and η under the different conditions. Specifically, Fig. 12 is for $A_0 = 1.5$, $w_{20} = 1$, $w_1 = -1.3$, $\omega = 0.35$, and $\alpha = 0.05$ for time $\tau = 0, 40, 50$, and 60 in the top row [Figs. 12(a1) to 12(a4)] and their Fourier transform in the momentum space $|\hat{\psi}(\vec{\beta}, \tau)|^2$ in the

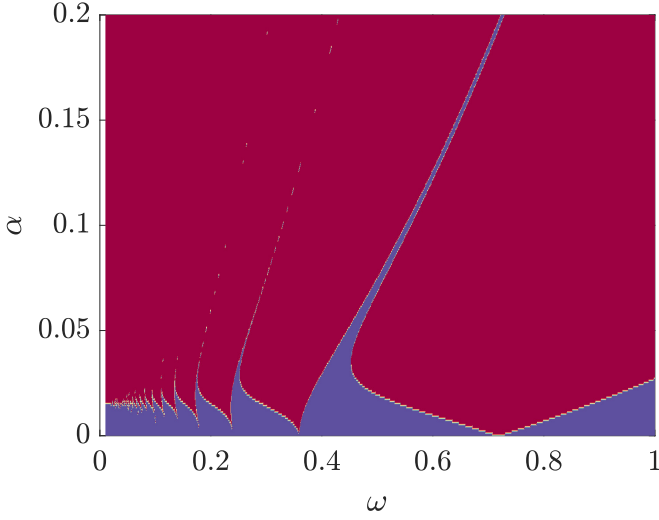


FIG. 11. Phase diagram of the domains of the FI (red regions) in the parameter space of the amplitude α and the frequency ω of the periodic drive with $w_2 = 1$, $w_{10} = -1$, $\beta = 2.73$, and $A_0 = 1.5$.

bottom row [Figs. 12(b1) to 12(b4)]. Here the red (blue) region represents the large (small) value. It can be seen that the homogenous density wave is modulated gradually to form the droplet structure.

When local nonlinearity w_1 is adjusted to -1.28 and other parameters are fixed, a new structure appears, which are shown in the top row in Fig. 13 for different time $\tau = 0, 75, 100$, and 150 , and the bottom row are for the corresponding results in momentum space. A new way to achieve the Faraday waves is to change the modulation frequency ω to 0.72 . Furthermore, the production of the new pattern is illustrated in Fig. 14 with $A_0 = 1.5$, $w_{20} = 1$, $w_1 = -1.2$, $\omega = 0.72$, and $\alpha = 0.05$.

V. DISCUSSION AND SUMMARY

To achieve such modulated parameters at current experiment conditions, on the one hand, we can modulate the

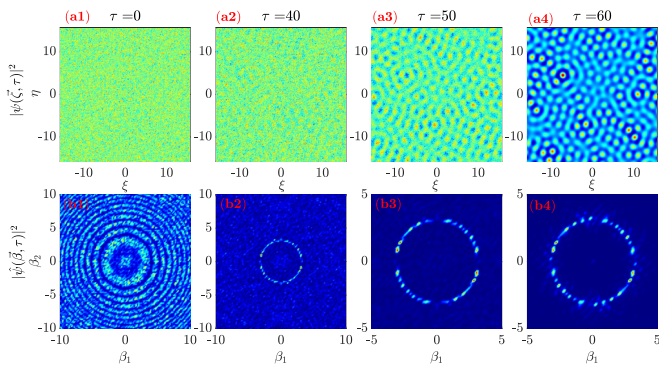


FIG. 12. Creation of two-dimensional density wave $|\psi(\vec{\zeta}, \tau)|^2$ by time-modulated periodically nonlocal interaction with $A_0 = 1.5$; $w_{20} = 1$, $w_1 = -1.3$, $\omega = 0.35$, and $\alpha = 0.05$ for different time $\tau = 0, 40, 50$, and 60 in (a1)–(a4), and that in the momentum space $|\hat{\psi}(\vec{\beta}, \tau)|^2$ with $\vec{\beta} \equiv (\beta_1, \beta_2)$ in (b1)–(b4), where the red (blue) region represents the large (small) value.

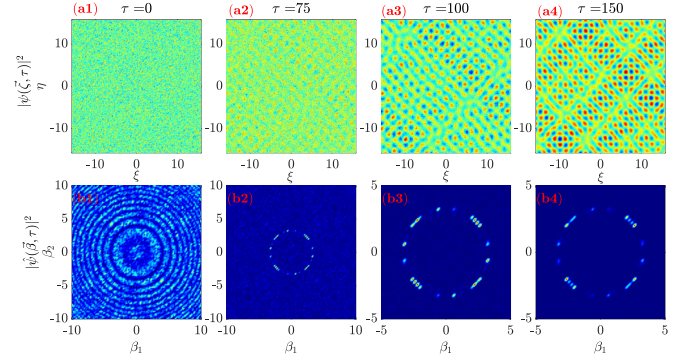


FIG. 13. Creation of two-dimensional density wave $|\psi(\vec{\zeta}, \tau)|^2$ by time-modulated periodically nonlocal interaction with $A_0 = 1.5$; $w_{20} = 1$, $w_1 = -1.28$, $\omega = 0.35$, and $\alpha = 0.05$ for different time $\tau = 0, 75, 100$, and 150 in (a1)–(a4), and that in the momentum space $|\hat{\psi}(\vec{\beta}, \tau)|^2$ in (b1)–(b4), where the red (blue) region represents the large (small) value.

parameter w_2 by adjusting the control laser field $\Omega_c \equiv \Omega_c(t)$ or dispersion parameters C_6 [47]. On the other hand, one can modulate the scattering length by means of Feshbach resonances [15,16,31–33]. Under these conditions and by setting suitable system parameters, the matter wave will undergo FI and then be transformed into the Faraday patterns along with the time.

In summary, we investigated both analytically and numerically the dynamics of Rydberg-dressed BECs subjected to periodic modulation of the nonlocal repulsive interactions in time through temporally modulated control laser field. We showed that the interactions may be tuned actively by utilizing such control laser field, and hence a plane-wave state of matter wave can undergo a RI and FI simultaneously or separately, depending on the choice of the system parameters. Based on Floquet stability analysis, we also found the evolution of small perturbations of the background allows the instability growth, thereby identifying instability regions with respect to density waves and among other modes of the system the roton mode is most effectively excited due to a significant contribution

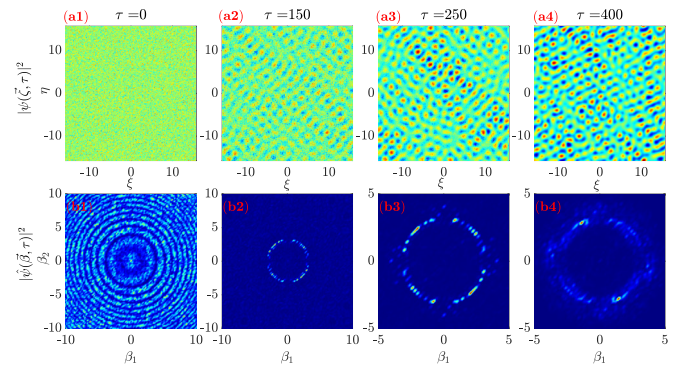


FIG. 14. Creation of two-dimensional density wave $|\psi(\vec{\zeta}, \tau)|^2$ by time-modulated periodically nonlocal interaction with $A_0 = 1.5$; $w_{20} = 1$, $w_1 = -1.2$, $\omega = 0.72$, and $\alpha = 0.05$ for different time $\tau = 0, 150, 250$, and 400 in (a1)–(a4), and that in the momentum space $|\hat{\psi}(\vec{\beta}, \tau)|^2$ with $\vec{\beta} \equiv (\beta_1, \beta_2)$ in (b1)–(b4), where the red (blue) region represents the large (small) value.

of subharmonics of the excitation frequency. From the direct numerical simulations of nonlocal GPE, we observed that the Faraday patterns emerge in a much shorter time both in one- and two-dimensional space. Finally, an interesting steady stand-wave in the condensate can persist after the creation even though canceling the modulation. These investigations enriched our understanding on the driven pattern formation mechanisms of the related pattern formation in systems with repulsive long-range interactions, which has the potential applications in fundamental physics along with various other practical implications.

ACKNOWLEDGMENTS

Z. Shi acknowledges the support of National Natural Science Foundation of China (Grant No. 12304357), Hubei Provincial Natural Science Foundation of China (Grant No. 2023AFB352), and a start-up fund from Hubei University of Automotive Technology (Grant No. BK202210). Y. Zhou acknowledges the support of Hubei Provincial Natural Science

Foundation of China (Grant No. 2023AFB891) and Chunhui Project Foundation of the Education Department of China (Grant No. HZKY20220337). L. Qin acknowledges the support of National Natural Science Foundation of China (Grant No. 12247146). F. Badshah acknowledges the support of a start-up fund from Hubei University of Automotive Technology (Grant No. BK202212).

APPENDIX A: DERIVATION NONLOCAL GP EQUATION IN RYDBERG-DRESSED BECs

We consider a system with N identical atoms whose center-of-mass motion is quantized. The atoms have multiple internal states $|\alpha\rangle$. The atomic annihilation operator is $\hat{\Psi}(\mathbf{r}) = \sum_{\alpha} \hat{\psi}_{\alpha}(\mathbf{r})|\alpha\rangle$ [$\hat{\Psi}^{\dagger}(\mathbf{r}) = \sum_{\alpha} \hat{\psi}_{\alpha}^{\dagger}(\mathbf{r})\langle\alpha|$] with $\hat{\psi}_{\alpha}(\mathbf{r})$ the annihilation operator of α th component ($\alpha = 1, 2, 3, \dots, M$). Here the base vectors are $|1\rangle = (1, 0, \dots, 0)^T$, $|2\rangle = (0, 1, \dots, 0)^T, \dots, |M\rangle = (0, \dots, 0, 1_M)^T$. The second-quantization Hamiltonian of the atoms is given by $\hat{H} = \hat{H}_0 + \hat{H}_{\text{int}}$, with

$$\hat{H}_0 = \int d^3r \hat{\Psi}^{\dagger}(\mathbf{r}) \left[-\frac{\hbar^2}{2m} \nabla^2 + V(\mathbf{r}) - \sum_{\alpha=1}^3 \hbar d_{\alpha} |\alpha\rangle\langle\alpha| - \hbar\Omega_p |2\rangle\langle 1| - \hbar\Omega_c |3\rangle\langle 2| + \text{H.c.} \right] \hat{\Psi}(\mathbf{r}), \quad (\text{A1a})$$

$$\hat{H}_{\text{int}} = \frac{1}{2} \iint d^3r d^3r' \sum_{\alpha, \beta=1}^3 \hat{\psi}_{\alpha}^{\dagger}(\mathbf{r}) \hat{\psi}_{\beta}^{\dagger}(\mathbf{r}') U_{\alpha\beta}(\mathbf{r}, \mathbf{r}') \hat{\psi}_{\beta}(\mathbf{r}') \hat{\psi}_{\alpha}(\mathbf{r}), \quad (\text{A1b})$$

where $d^3r = dx dy dz$ and $d_{\alpha} = \Delta_{\alpha} + i\gamma_{\alpha}/2$ ($\alpha = 1, 2, 3$). From the Heisenberg equation of motion $i\hbar \frac{\partial}{\partial t} \hat{\Psi}(\mathbf{r}, t) = [\hat{\Psi}(\mathbf{r}, t), \hat{H}] + i\hat{F}$ with $\hat{F} = \sum_{\alpha=1}^3 \hat{F}_{\alpha}|\alpha\rangle$ noise operator, we obtain

$$i\hbar \frac{\partial}{\partial t} \hat{\psi}_1 = \left(-\frac{\hbar^2}{2m} \nabla^2 + V(\mathbf{r}) - \hbar d_1 \right) \hat{\psi}_1 - \hbar\Omega_p \hat{\psi}_2 + \sum_{\beta} \int d^3r' U_{1\beta}(\mathbf{r}, \mathbf{r}') \hat{\psi}_{\beta}^{\dagger}(\mathbf{r}') \hat{\psi}_{\beta}(\mathbf{r}') \hat{\psi}_1(\mathbf{r}) + i\hat{F}_1, \quad (\text{A2a})$$

$$i\hbar \frac{\partial}{\partial t} \hat{\psi}_2 = \left(-\frac{\hbar^2}{2m} \nabla^2 + V(\mathbf{r}) - \hbar d_2 \right) \hat{\psi}_2 - \hbar\Omega_p \hat{\psi}_1 - \hbar\Omega_c^* \hat{\psi}_3 + \sum_{\beta} \int d^3r' U_{2\beta}(\mathbf{r}, \mathbf{r}') \hat{\psi}_{\beta}^{\dagger}(\mathbf{r}') \hat{\psi}_{\beta}(\mathbf{r}') \hat{\psi}_2(\mathbf{r}) + i\hat{F}_2, \quad (\text{A2b})$$

$$i\hbar \frac{\partial}{\partial t} \hat{\psi}_3 = \left(-\frac{\hbar^2}{2m} \nabla^2 + V(\mathbf{r}) - \hbar d_3 \right) \hat{\psi}_3 - \hbar\Omega_c \hat{\psi}_2 + \sum_{\beta} \int d^3r' U_{3\beta}(\mathbf{r}, \mathbf{r}') \hat{\psi}_{\beta}^{\dagger}(\mathbf{r}') \hat{\psi}_{\beta}(\mathbf{r}') \hat{\psi}_3(\mathbf{r}) + i\hat{F}_3. \quad (\text{A2c})$$

Note that the above model includes the atom-atom interactions between all internal states. For simplicity, we assume that for atom-atom interaction only two parameters U_{11} and U_{33} are nonzero. Then the above equations are reduced into

$$i\hbar \frac{\partial}{\partial t} \hat{\psi}_1 = \left(-\frac{\hbar^2}{2m} \nabla^2 + V(\mathbf{r}) - \hbar d_1 \right) \hat{\psi}_1 - \hbar\Omega_p \hat{\psi}_2 + \int d^3r' U_{11}(\mathbf{r}, \mathbf{r}') \hat{\psi}_1^{\dagger}(\mathbf{r}', t) \hat{\psi}_1(\mathbf{r}', t) \hat{\psi}_1(\mathbf{r}, t) + i\hat{F}_1, \quad (\text{A3a})$$

$$i\hbar \frac{\partial}{\partial t} \hat{\psi}_2 = \left(-\frac{\hbar^2}{2m} \nabla^2 + V(\mathbf{r}) - \hbar d_2 \right) \hat{\psi}_2 - \hbar\Omega_p \hat{\psi}_1 - \hbar\Omega_c^* \hat{\psi}_3 + i\hat{F}_2, \quad (\text{A3b})$$

$$i\hbar \frac{\partial}{\partial t} \hat{\psi}_3 = \left(-\frac{\hbar^2}{2m} \nabla^2 + V(\mathbf{r}) - \hbar d_3 \right) \hat{\psi}_3 - \hbar\Omega_c \hat{\psi}_2 + \int d^3r' U_{33}(\mathbf{r}, \mathbf{r}') \hat{\psi}_3^{\dagger}(\mathbf{r}', t) \hat{\psi}_3(\mathbf{r}', t) \hat{\psi}_3(\mathbf{r}, t) + i\hat{F}_3, \quad (\text{A3c})$$

where the term related to U_{11} is due to the mean-field interaction between the atoms in the BEC, while term related to U_{33} is due to the Rydberg-Rydberg interaction between the atoms at Rydberg states. In the following the time variable t in $\hat{\psi}_{\alpha}$ will be omitted for simplicity. Assuming $\hbar d_2$ and $\hbar d_3$ are large, we have

$$d_2 \hat{\psi}_2 \approx -\Omega_p \hat{\psi}_1 + \Omega_c^* \hat{\psi}_3, \quad \hbar d_3 \hat{\psi}_3 \approx \int d^3r' U_{33}(\mathbf{r}, \mathbf{r}') \hat{\psi}_3^{\dagger}(\mathbf{r}') \hat{\psi}_3(\mathbf{r}') \hat{\psi}_3(\mathbf{r}) - \hbar\Omega_c \hat{\psi}_2. \quad (\text{A4})$$

Since the interaction $U_{33}(\mathbf{r}, \mathbf{r}')$ changes much slowly than that of the operator $\hat{\psi}_1(\mathbf{r}')$, and the particles populate mainly in ground state $|1\rangle$, and applying the iteration method to Eqs. (A4), we have

$$\begin{aligned} \hat{\psi}_2 &= \hat{\psi}_2^{(1)} + \hat{\psi}_2^{(3)} + \hat{\psi}_2^{(5)} \\ &\approx -\frac{d_3}{D}\Omega_p\hat{\psi}_1 - \frac{|\Omega_c|^4|\Omega_p|^2\Omega_p}{\hbar|D|^4} \\ &\quad \times \int \frac{d^3r'U_{33}(\mathbf{r}, \mathbf{r}')\hat{\psi}_1^\dagger(\mathbf{r}')\hat{\psi}_1(\mathbf{r}')\hat{\psi}_1(\mathbf{r})}{1 + Nd_2|\Omega_c|^2|\Omega_p|^2U_{33}(\mathbf{r}, \mathbf{r}')/(\hbar|D|^2D)}, \end{aligned} \quad (\text{A5})$$

where $D = d_2d_3 - |\Omega_c|^2$. Substituted Eq. (A5) into Eq. (A3a), it gives the closure equation about $\hat{\psi}_1$:

$$\begin{aligned} i\hbar\frac{\partial}{\partial t}\hat{\psi}_1 &= \left(-\frac{\hbar^2}{2m}\nabla^2 + V(\mathbf{r}) - \hbar d_1\right)\hat{\psi}_1 + \frac{\hbar d_3|\Omega_p|^2}{D}\hat{\psi}_1 \\ &\quad + \int d^3r'U_{11}(\mathbf{r}, \mathbf{r}')\hat{\psi}_1^\dagger(\mathbf{r}')\hat{\psi}_1(\mathbf{r}')\hat{\psi}_1(\mathbf{r}) + i\hat{F}_1 \\ &\quad + \int d^3r'\frac{\hbar|\Omega_c|^4|\Omega_p|^4U_{33}(\mathbf{r}, \mathbf{r}')\hat{\psi}_1^\dagger(\mathbf{r}')\hat{\psi}_1(\mathbf{r}')\hat{\psi}_1(\mathbf{r})}{\hbar|D|^4 + Nd_2|\Omega_c|^2|\Omega_p|^2D^*U_{33}(\mathbf{r}, \mathbf{r}')}. \end{aligned} \quad (\text{A6})$$

We now apply the Bogoliubov ansatz [46] $\hat{\psi}_1(\mathbf{r}) = \psi_1(\mathbf{r}) + \hat{\phi}_1(\mathbf{r})$. Here $\psi_1(\mathbf{r}) = \langle\hat{\psi}_1(\mathbf{r})\rangle$ is the so-called condensate wave function, a classical field that represents the wave function of particles in the BECs, which is normalized to $\langle\psi_1|\psi_1\rangle = \int d^3r|\psi_1(\mathbf{r})|^2 = N$. $\hat{\phi}_1(\mathbf{r})$ describes fluctuations and vanishes on average $\langle\hat{\phi}_1(\mathbf{r})\rangle = 0$. Eventually, by using the mean-field approximation, we have

$$\begin{aligned} i\hbar\frac{\partial}{\partial t}\psi_1 &= \left(-\frac{\hbar^2}{2m}\nabla^2 + V(\mathbf{r}) - \hbar d_1\right)\psi_1 + \frac{\hbar d_3|\Omega_p|^2}{D}\psi_1 \\ &\quad + \int d^3r'U_{11}(\mathbf{r}, \mathbf{r}')|\psi_1(\mathbf{r}')|^2\psi_1(\mathbf{r}) \\ &\quad + \int d^3r'\frac{\hbar|\Omega_c|^4|\Omega_p|^4U_{33}(\mathbf{r}, \mathbf{r}')|\psi_1(\mathbf{r}')|^2\psi_1(\mathbf{r})}{\hbar|D|^4 + Nd_2|\Omega_c|^2|\Omega_p|^2D^*U_{33}(\mathbf{r}, \mathbf{r}')}, \end{aligned} \quad (\text{A7})$$

where $U_{33}(\mathbf{r}, \mathbf{r}') = \hbar C_6/|\mathbf{r} - \mathbf{r}'|^6$, $d_1 = \Delta_1 + i\gamma_1/2 \approx 0$, and $U_{11}(\mathbf{r}, \mathbf{r}') = W\delta(\mathbf{r} - \mathbf{r}')$ with $W = 4\pi\hbar^2 a/m$. We can convert Eq. (A7) into

$$\begin{aligned} i\hbar\frac{\partial}{\partial t}\psi_1 &= \left(-\frac{\hbar^2}{2m}\nabla^2 + V(\mathbf{r})\right)\psi_1 + \frac{\hbar d_3|\Omega_p|^2}{D}\psi_1 \\ &\quad + W|\psi_1(\mathbf{r}')|^2\psi_1(\mathbf{r}) + \int d^3r'\frac{\hbar\tilde{C}_6|\psi_1(\mathbf{r}')|^2\psi_1(\mathbf{r})}{R_c^6 + |\mathbf{r} - \mathbf{r}'|^6}. \end{aligned} \quad (\text{A8})$$

Introducing $\Psi = \psi_1 \exp\{id_3|\Omega_p|^2t/D\}$, we have

$$\begin{aligned} i\hbar\frac{\partial}{\partial t}\Psi &= \left[-\frac{\hbar^2}{2m}\nabla^2 + V + W|\Psi(\mathbf{r})|^2\right. \\ &\quad \left.+ \int d^3r'\frac{\hbar\tilde{C}_6|\Psi(\mathbf{r}')|^2}{R_c^6 + |\mathbf{r} - \mathbf{r}'|^6}\right]\Psi, \end{aligned} \quad (\text{A9})$$

where $\tilde{C}_6 = \frac{|\Omega_c|^4|\Omega_p|^4}{|D|^4}C_6$ and $R_c^6 = \frac{NC_6d_2|\Omega_c|^2|\Omega_p|^2}{|D|^2D}$.

APPENDIX B: FLOQUET ANALYSIS FOR FARADAY INSTABILITY

In the main text, we obtained the Mathieu-type equation for B_1 , i.e.,

$$\frac{d^2\tilde{B}_1}{d\tau^2} + [\lambda^2 + 2\alpha A_0^2 w_{20}\beta^2 \mathcal{U}_{1D}(\beta) \cos(2\omega\tau)]\tilde{B}_1 = 0. \quad (\text{B1})$$

Equation (B1) can be written into the form of system of two first-order ordinary differential equations,

$$\frac{d}{d\tau}\begin{bmatrix} B_1 \\ B'_1 \end{bmatrix} = \begin{bmatrix} 0 & 1 \\ -f(\tau) & 0 \end{bmatrix}\begin{bmatrix} B_1 \\ B'_1 \end{bmatrix}, \quad (\text{B2})$$

where $B'_1 = dB_1/d\tau$, and $f(\tau) = -\lambda^2 + 2A_0^2\alpha\beta^2\mathcal{U}_{1D}\cos(2\omega\tau)$. We note that the coefficient matrix is periodic with period $T = \pi/\omega$. Using Floquet theory, we create a fundamental solution matrix M with the form

$$M = \begin{bmatrix} b_{i1}(T) & b_{j1}(T) \\ b_{i2}(T) & b_{j2}(T) \end{bmatrix}, \quad (\text{B3})$$

where $b_{i1}(T)$, $b_{i2}(T)$ and $b_{j1}(T)$, $b_{j2}(T)$ are, respectively, the two fundamental solution vectors of B_i and B_j . Furthermore, the initial conditions B_i and B_j satisfy that $B_i = (1, 0)$ and $B_j = (0, 1)$. We now solve for the eigenvalues of M by the characteristic equation for matrix M ,

$$\kappa^2 - \text{Tr}(M)\kappa + \text{Det}(M) = 0. \quad (\text{B4})$$

It is easy to show that the $d\text{Det}(M)/d\tau = 0$, thus we obtain $\text{Det}(M) = 1$. The characteristic Eq. (B4) becomes

$$\kappa^2 - \text{Tr}(M)\kappa + 1 = 0. \quad (\text{B5})$$

We hence have $\kappa_{1,2} = \frac{\text{Tr}(M) \pm \sqrt{\text{Tr}(M)^2 - 4}}{2}$ and $\kappa_1\kappa_2 = 1$. Any $\kappa_{1,2} > 1$ indicates instability. Thus we have the neutrally stable domain by $|\text{Tr}(M)| = 2$. Based on the proposed theoretical approach, it allows one to identify the domains of instability in the parameter space by numerical integration the Eq. (B2) in the interval $[0, T]$ and to find the critical domain by Eq. (B5).

- [1] M. C. Cross and P. C. Hohenberg, Pattern formation outside of equilibrium, *Rev. Mod. Phys.* **65**, 851 (1993).
 [2] C. Bowman and A. C. Newell, Natural patterns and wavelets, *Rev. Mod. Phys.* **70**, 289 (1998).

- [3] H. Bénard, Les tourbillons cellulaires dans une nappe liquide. Méthodes optiques d'observation et d'enregistrement, *J. Phys. Theor. Appl.* **10**, 254 (1901).
 [4] P. G. Drazin and W. H. Reid, *Hydrodynamic Stability* (Cambridge University Press, Cambridge, England, 1981).

- [5] G. I. Taylor, Stability of a viscous liquid contained between two rotating cylinders, *Philos. Trans. R. Soc. London, Ser. A* **223**, 289 (1923).
- [6] E. Dubois-Violette, G. Durand, E. Guyon, P. Manneville, and P. Pieranski, *Solid State Physics* (Academic Press, New York, 1978), p. 147.
- [7] M. Faraday, XVII. On a peculiar class of acoustical figures; and on certain forms assumed by groups of particles upon vibrating elastic surfaces, *Philos. Trans. R. Soc.* **121**, 299 (1831).
- [8] A. C. Newell and J. V. Moloney, *Nonlinear Optics* (Addison-Wesley, Reading, MA, 1990).
- [9] F. T. Arecchi, S. Boccaletti, and P. Ramazza, Pattern formation and competition in nonlinear optics, *Phys. Rep.* **318**, 1 (1999).
- [10] L. A. Lugiato, M. Brambilla, and A. Gatti, Optical pattern formation, *Adv. At. Mol. Opt. Phys.* **40**, 229 (1999).
- [11] W. W. Mullins and R. F. Sekerka, Stability of planar interface during solidification of a dilute binary alloy, *J. Appl. Phys.* **35**, 444 (1964).
- [12] A. M. Turin, The chemical basis of morphogenesis, *Philos. Trans. R. Soc. London B* **237**, 37 (1952).
- [13] J. J. García-Ripoll, V. M. Perez-Garcia, and P. Torres, Extended parametric resonances in nonlinear schrodinger systems, *Phys. Rev. Lett.* **83**, 1715 (1999).
- [14] C. Schori, T. Stoferle, H. Moritz, M. Kohl, and T. Esslinger, Excitations of a superfluid in a three-dimensional optical lattice, *Phys. Rev. Lett.* **93**, 240402 (2004).
- [15] K. Staliunas, S. Longhi, and G. J. de Valcarcel, Faraday patterns in Bose-Einstein condensates, *Phys. Rev. Lett.* **89**, 210406 (2002).
- [16] K. Staliunas, S. Longhi, and G. J. de Valcarcel, Faraday patterns in low-dimensional Bose-Einstein condensates, *Phys. Rev. A* **70**, 011601(R) (2004).
- [17] K. Kwon, K. Mukherjee, S. J. Huh, K. Kim, S. I. Mistakidis, D. K. Maity, P. G. Kevrekidis, S. Majumder, P. Schmelcher, and J.-Y. Choi, Spontaneous formation of star-shaped surface patterns in a driven Bose-Einstein condensate, *Phys. Rev. Lett.* **127**, 113001 (2021).
- [18] A. Balaž, R. Paun, A. I. Nicolin, S. Balasubramanian, and R. Ramaswamy, Faraday waves in collisionally inhomogeneous Bose-Einstein condensates, *Phys. Rev. A* **89**, 023609 (2014).
- [19] T. Chen, K. Shibata, Y. Eto, T. Hirano, and H. Saito, Faraday patterns generated by Rabi oscillation in a binary Bose-Einstein condensate, *Phys. Rev. A* **100**, 063610 (2019).
- [20] A. Balaž and A. I. Nicolin, Faraday waves in binary non-miscible Bose-Einstein condensates, *Phys. Rev. A* **85**, 023613 (2012).
- [21] M. Silber, C. M. Topaz, and A. C. Skeldon, Two-frequency forced Faraday waves: Weakly damped modes and pattern selection, *Physica D* **143**, 205 (2000).
- [22] J. Porter and M. Silber, Broken symmetries and pattern formation in two-frequency forced faraday waves, *Phys. Rev. Lett.* **89**, 084501 (2002).
- [23] K. Łakomy, R. Nath, and L. Santos, Faraday patterns in coupled one-dimensional dipolar condensates, *Phys. Rev. A* **86**, 023620 (2012).
- [24] B. Kh. Turmanov, B. B. Baizakov, F. Kh. Abdullaev, and M. Salerno, Oscillations of a quasi-one-dimensional dipolar supersolid, *J. Phys. B: At. Mol. Opt. Phys.* **54**, 145302 (2021).
- [25] F. Kh. Abdullaev, M. Ogren, and M. P. Sorensen, Faraday waves in quasi-one-dimensional superfluid Fermi-Bose mixtures, *Phys. Rev. A* **87**, 023616 (2013).
- [26] T. F. Gallagher, *Rydberg Atoms* (Springer, New York, 2006).
- [27] M. Saffman, T. G. Walker, and K. Molmer, Quantum information with Rydberg atoms, *Rev. Mod. Phys.* **82**, 2313 (2010).
- [28] C. S. Adams, J. D. Pritchard, and J. P. Shaffer, Rydberg atom quantum technologies, *J. Phys. B: At. Mol. Opt. Phys.* **53**, 012002 (2019).
- [29] A. W. Glaetzle, M. Dalmonte, R. Nath, I. Rouschatzakis, R. Moessner, and P. Zoller, Quantum spin-ice and dimer models with Rydberg atoms, *Phys. Rev. X* **4**, 041037 (2014).
- [30] T. Keating, K. Goyal, Y.-Y. Jau, G. W. Biedermann, A. J. Landahl, and I. H. Deutsch, Adiabatic quantum computation with Rydberg-dressed atoms, *Phys. Rev. A* **87**, 052314 (2013).
- [31] M. Theis, G. Thalhammer, K. Winkler, M. Hellwig, G. Ruff, R. Grimm, and J. Hecker Denschlag, Tuning the scattering length with an optically induced Feshbach resonance, *Phys. Rev. Lett.* **93**, 123001 (2004).
- [32] A. Marte, T. Volz, J. Schuster, S. Durr, G. Rempe, E. G. M. van Kempen, and B. J. Verhaar, Feshbach resonances in rubidium 87: Precision measurement and analysis, *Phys. Rev. Lett.* **89**, 283202 (2002).
- [33] C. Chin, R. Grimm, P. Julienne, and E. Tiesinga, Feshbach resonances in ultracold gases, *Rev. Mod. Phys.* **82**, 1225 (2010).
- [34] D. A. Steck, Rubidium 87 D Line Data, <http://steck.us/alkalidata>.
- [35] K. Singer, J. Stanojevic, M. Weidemuller, and R. Cote, Long-range interactions between alkali Rydberg atom pairs correlated to the ns-ns, np-np and nd-nd asymptotes, *J. Phys. B: At. Mol. Opt. Phys.* **38**, S295 (2005).
- [36] N. Henkel, R. Nath, and T. Pohl, Three-dimensional roton excitations and supersolid formation in Rydberg-excited Bose-Einstein condensates, *Phys. Rev. Lett.* **104**, 195302 (2010).
- [37] F. Cinti, P. Jain, M. Boninsegni, A. Micheli, P. Zoller, and G. Pupillo, Supersolid droplet crystal in a dipole-blockaded gas, *Phys. Rev. Lett.* **105**, 135301 (2010).
- [38] N. Henkel, F. Cinti, P. Jain, G. Pupillo, and T. Pohl, Supersolid vortex crystals in Rydberg-dressed Bose-Einstein condensates, *Phys. Rev. Lett.* **108**, 265301 (2012).
- [39] C.-H. Hsueh, T.-C. Lin, T.-L. Horng, and W. C. Wu, Quantum crystals in a trapped Rydberg-dressed Bose-Einstein condensate, *Phys. Rev. A* **86**, 013619 (2012).
- [40] C.-H. Hsueh, Y.-C. Tsai, K.-S. Wu, M.-S. Chang, and W. C. Wu, Pseudospin orders in the supersolid phases in binary Rydberg-dressed Bose-Einstein condensates, *Phys. Rev. A* **88**, 043646 (2013).
- [41] Z. Shi and G. Huang, Selection and cloning of periodic optical patterns with a cold Rydberg atomic gas, *Opt. Lett.* **46**, 5344 (2021).
- [42] F. Maucher, T. Pohl, S. Skupin, and W. Krolikowski, Self-organization of light in optical media with competing nonlinearities, *Phys. Rev. Lett.* **116**, 163902 (2016).
- [43] Z. Shi, W. Li, and G. Huang, Structural phase transitions of optical patterns in atomic gases with microwave-controlled Rydberg interactions, *Phys. Rev. A* **102**, 023519 (2020).

- [44] Z. Shi and G. Huang, Self-organized structures of two-component laser fields and their active controls in a cold Rydberg atomic gas, *Phys. Rev. A* **104**, 013511 (2021).
- [45] L. D. Landau and E. M. Lifshitz, *Mechanics* (Pergamon, Oxford, 1976).
- [46] S. Ronen and J. L. Bohn, Dipolar Bose-Einstein condensates at finite temperature, *Phys. Rev. A* **76**, 043607 (2007).
- [47] C. L. Vaillant, M. P. A. Jones, and R. M. Potvliege, Long-range Rydberg-Rydberg interactions in calcium, strontium and ytterbium, *J. Phys. B: At. Mol. Opt. Phys.* **45**, 135004 (2012).